Reaching for Mechanistic Consensus Across Life Kingdoms: Structure and Insights into Catalysis of the *myo*-Inositol-1-phosphate Synthase (mIPS) from *Archaeoglobus fulgidus*[†,‡]

Kimberly A. Stieglitz,[§,||] Hongying Yang,[||] Mary F. Roberts,[||] and Boguslaw Stec*[,§]

Department of Chemistry, University of Texas at El Paso, El Paso, Texas 79968, and Department of Chemistry, Merkert Chemistry Center, Boston College, Chestnut Hill, Massachusetts 02467

Received August 11, 2004; Revised Manuscript Received October 25, 2004

ABSTRACT: *myo*-Inositol-1-phosphate synthase (mIPS) catalyzes the first step in the synthesis of L-*myo*-inositol-1-phosphate. We have solved and refined the structure of the mIPS from the hyperthermophilic sulfate reducer *Archaeoglobus fulgidus* at 1.9 Å resolution. The enzyme crystallized from poly(ethylene glycol) in the *P*1 space group with one tetramer in the asymmetric unit and provided a view of the entire biologically active oligomer. Despite significant changes in sequence length and amino acid composition, the general architecture of the archaeal enzyme is similar to that of the eukaryotic mIPS from *Saccharomyces cerevisiae* and bacterial mIPS from *Mycobacterium tuberculosis*. The enhanced thermostability of the archaeal enzyme as compared to that from yeast is consistent with deletion of a number of surface loops that results in a significantly smaller protein. In the structure of the *A. fulgidus* mIPS, the active sites of all four subunits were fully ordered and contained NAD^+ and inorganic phosphate. The structure also contained a single metal ion (identified as K^+) in two of the four subunits. The analysis of the electrostatic potential maps of the protein suggested the presence of a second metal-ion-binding site in close proximity to the first metal ion and NAD^+. The modeling of the substrate and known inhibitors suggests a critical role for the second metal ion in catalysis and provides insights into the common elements of the catalytic cycle in enzymes from different life kingdoms.

Inositol plays an important physiological role in a very wide range of organisms. In eukaryotes, inositol as a component of phosphoinositides constitutes a critical element in signal transduction pathways (*1*, *2*). In bacteria and archaea, molecules containing this moiety are involved in the response to external stress (*3*, *4*). The only known *de novo* biosynthetic pathway of inositol synthesis involves the conversion of D-glucose 6-phosphate (G-6-P)[1] to L-*myo*-inositol-1-phosphate (I-1-P), followed by hydrolysis of I-1-P to *myo*-inositol by inositol monophosphatase. Production of I-1-P by *myo*-inositol-1-phosphate synthase (mIPS) is both the rate limiting and committed step in inositol biosynthesis (*5*).

mIPS has been cloned from many species including insects, plants, yeast, human, and the hyperthermophilic archaeon *Archaeoglobus fulgidus*. Unlike the eukaryotic and bacterial mIPS, the enzyme from *A. fulgidus* is exceptionally thermostable and its activity is absolutely dependent on the presence of the metal ions (*6*). The sequence similarity would suggest a common catalytic mechanism with the well-studied yeast mIPS. However, the demonstrated dependence of the archaeal enzyme on metal ions suggests that the catalytic mechanism of archaeal mIPS is significantly different from that of the eukaryotic homologues.

Biochemical studies have suggested the general outline of the catalytic reaction (*5*, *7*, *8*). mIPS initiates the reaction by binding the acyclic tautomer of the G-6-P. This linearized glucose is oxidized to 5-keto-G-6-P with concomitant reduction of NAD^+. Both the 5-keto-G-6-P and the NADH are tightly bound by the enzyme. Subsequent enolization of the oxidized substrate and intramolecular aldol cyclization yield the second tightly bound intermediate, *myo*-2-inosose-1-phosphate. Reduction of the inosose compound by the bound NADH produces I-1-P and regenerates NAD^+. The yeast enzyme is activated by ammonium ions that are thought to help stabilize the transition state for cyclization (*5*). The fact that the *A. fulgidus* mIPS is not activated by NH_4^+ but by divalent cations (*6*) suggests it is a type-II aldolase, where a divalent cation such as Zn^{2+} or Mg^{2+} acts as a Lewis acid to stabilize the transition state (*8*, *9*). It is quite common that different enzymes use a very similar catalytic mechanism, but it is quite unusual that the same enzyme in different species (especially ones with significant homology) would use two distinctly different mechanisms to carry out the same reaction.

Recently, two mIPS crystal structures have been solved (*10*, *11*). The structure of the yeast enzyme with bound

[†] This work has been supported by NIH Grant 1R01 GM64481 (to B.S.), National Science Foundation Grant MCB-9978250 (to M.F.R.), and Department of Energy Biosciences DE-FG02-91ER20025 (to M.F.R.).

[‡] The PDB code for the coordinate files is 1U1I.

* To whom correspondence should be addressed. E-mail: bstec@utep.edu. Telephone: 915-747-7576. Fax: 915-747-5748.

[§] University of Texas at El Paso.

[||] Boston College.

[1] Abbreviations: mIPS, *myo*-inositol-1-phosphate synthase; G-6-P, D-glucose-6-phosphate; I-1-P, L-*myo*-inositol-1-phosphate; dgtolP, 2-deoxy-D-glucitol-6-(*E*)-vinyl-homophosphonate; rmsd, root-mean-square deviation.

10.1021/bi048267o CCC: $30.25
Published on Web 12/10/2004

NAD^+ and dgtolP, an inhibitor that mimics the linearized G-6-P, has provided the most detailed view of the mIPS active site. An initial report described two structures of the yeast enzyme. One with only partial occupancy of NAD^+ had 60 residues disordered (351−409) that became ordered in the second structure with the inhibitor bound. This disordered structure was used to argue for "induced fit" by the substrates where it was thought the enzyme refolded to encapsulate the substrate (*10*). The *M. tuberculosis* mIPS clearly showed density for the NAD^+ in the absence of a substrate analogue (*11*). It also contained bound metal ions that were putatively identified as Zn^{2+}. A subsequent, more thorough examination of the yeast mIPS structures with reduced and oxidized forms of NAD^+ identified a metal ion that appeared to help anchor the NAD^+ (*12*, *13*) in an analogous position to that in the *M. tuberculosis* enzyme. However, neither the yeast nor the bacterial mIPS enzymes are inhibited by ethylenediaminetetraacetic acid (EDTA), implying that if it is a divalent metal ion, then that ion is not critical for catalysis.

To resolve the mechanistic controversy concerning metal ions and to investigate further the details of the mechanism for mIPS, we have solved the structure of mIPS from the thermophilic sulfate reducer *A. fulgidus*. A comparison of the *A. fulgidus* mIPS structure with those of the enzyme from *S. cerevisiae* (*10*) and *M. tuberculosis* (*11*) provides unique insights into the catalytic mechanism and allows us to formulate unifying principles for catalysis by this class of enzymes. The structure obtained for *A. fulgidus* mIPS also helps to define a role for metal ions in the catalytic mechanism of this particular mIPS. Significant structural changes as compared to the yeast mIPS also highlight features responsible for the thermostability of the archaeal enzyme.

MATERIALS AND METHODS

Materials. NAD^+, G-6-P, and *myo*-inositol were purchased from Sigma. All other chemicals used were of reagent grade.

Expression and Purification of mIPS. Recombinant plasmid pBC/IPS1 containing the *A. fulgidus* sequence was transformed into BL21(DE3)pLysS cells and overexpressed and purified as described previously (*6*). Pure mIPS was dialyzed against 50 mM Tris at pH 7.5, with 1 mM EDTA, and then concentrated to 20 mg/mL. Protein concentration was measured by A_{280} [using e_{280} (0.1% w/v) = 1.149] as well as by the Lowry assay (*14*). Enzyme activity was checked by the ^{31}P NMR assay as described previously (*6*). Expression of the recombinant yeast mIPS was similar to that of the archaeal enzyme; protein was purified to >95% with two chromatographic steps (Q-sepharose Fast Flow followed by phenyl sepharose columns).

Crystallization. Purified, pooled, and concentrated enzyme was crystallized from two separate stock concentrations: 8.0 and 16 mg/mL. Crystals, obtained directly from the HR110 Hampton Screening kit, grew from HEPES at pH 7.5, 2% (v/v) poly(ethylene glycol) (PEG) 400, 2.0 M ammonium sulfate, and 30% (w/v) PEG 1500 in a 1:1 combination (*15*). The mIPS crystals appeared after 2 weeks and grew slowly to full size (0.5 × 0.4 × 0.4 mm) in approximately 3 weeks.

X-ray Data Collection. Crystals were mounted in glass capillaries directly from the crystallization wells. Data were collected at Rice University using a Rigaku H3R rotating anode generator with an R-AXIS IV++ imaging plate detector. The data were indexed and reduced using Crystal Clear software (MSC-Rigaku) in the *P*1 space group with unit cell dimensions 62.77, 83.94, and 91.79 Å and 65.79°, 72.43°, and 74.98°. The best crystals diffracted to approximately 1.9 Å resolution and gave a data set approximately 74% complete with $R_{merge} = 0.045$.

Structural Solution and Refinement. We initially attempted to solve the phase problem by using MIR and MAD methods. A single Fe^{2+} derivative was highly nonisomorphous (different cell dimensions and high interset R_{merge}), and crystals from the protein labeled with selenomethionine diffracted very weakly and appeared to have a different space group. Fortuitously, at the time, we initiated the heavy-atom work; the structure of yeast and then *M. tuberculosis* mIPS enzymes were published (*10*, *11*). Thus, we were able to solve the phasing problem by a combination of a single heavy atom with molecular replacement (*16*). A truncated polyalanine model derived from the yeast structure was used as the probe structure (*17*). The initial refinement was carried out by simulated annealing methodology as implemented in CNS (*18*). The model was then refined using Shelx-97 (*19*). The manual rebuilding sessions were carried out with XtalView (*20*) on a Linux workstation.

Sequence and Structural Alignments. Along with previous sequence alignments of mIPS from different species (*5*, *10*), we have carried out the structural alignment of known structures in Sequoia (*21*). Sequoia uses an iterative procedure to expand the initial alignment by fulfilling the prespecified geometrical conditions for the extension to produce a sequence alignment as well as structural superposition.

Modeling and Electrostatic Field Calculation. The initial energy optimization was carried out in CNS. The final stages of the modeling were carried out in Quanta (Accelrys, Inc). The electrostatic field calculations were done in GRASP. Visualization of the structures and the electrostatic field was used to locate the most probable binding site for a second metal ion.

Thermostability of A. fulgidus and E. coli mIPS. Thermostability of *A. fulgidus* mIPS was investigated by short-time single-concentration assays. The half-life of the enzyme for the loss of activity was estimated at 98 °C in 50 mM Tris-HCl at pH 8.0. Subsequently, the influence of 1 mM cofactor NAD^+ and 5 mM G-6-P on the thermal stability of the enzyme was investigated. Similar studies were carried out on recombinant yeast mIPS (L. Chen and M. F. Roberts, unpublished results) at 55 °C.

RESULTS AND DISCUSSION

Structure Solution versus Quality of the Data. Several data sets were collected, and the one with the highest resolution and lowest R_{merge} values was selected for the refinement (see Table 1 for statistics of the data collection and structure refinement). The data set of 92 869 reflections selected for the refinement was 74% complete to 1.9 Å resolution. The completeness in the lower resolution shell was also limited with the highest completeness of 87% at around 3.0 Å. Because the different data sets had significantly different cell dimensions, merging of data sets to improve completeness

Table 1: Data Collection and Refinement Statistics for *A. fulgidus* mIPS

resolution (Å)	1.90
number of total reflections	92 869
completeness (%)	74 (87)[a]
R_{sym}[b]	0.045
space group	*P*1
cell dimensions (Å)	$a = 62.77$, $b = 83.94$, c = 91.79
	$\alpha = 65.79$ $\beta = 72.43$, $\gamma = 74.98$
R/R_{free}[c,d]	0.216(0.213)/0.266(0.269)
average *B* factor (Å^2)	35.77
number of water molecules	1019
rmsd of bond lengths (Å)	0.005
rmsd of bond angles (deg)	27.517
rmsd dihedrals	1.168
rmsd impropers	1.621
number of residues	1568

[a] The highest completeness is reported at 3.0 Å. [b] $R_{sym} = (\sum||I| - |\langle I\rangle||)/(\sum|I|)$, where I is the observed intensity and $\langle I\rangle$ is the average intensity obtained from multiple observations of symmetry-related reflections. [c] $R = (\sum||F_{obs}| - |F_{cal}||)/(\sum|F_{obs}|)$. [d] $R_{free} = (\sum||F_{obs}| - |F_{cal}||)/(\sum|F_{obs}|)$, where reflections belong to a test set of 10% randomly selected data. R_{free} is reported in parentheses.

resulted in unacceptable increases in R_{merge}. The structure was solved by molecular replacement using a trial structure of a polyalanine tetramer that was derived from a truncated model of the yeast enzyme. The solution was unique and coincided in orientation with a general outline of the envelope obtained from a single derivative after implementation of a solvent-flattening procedure. The solution obtained was optimized by rounds of rigid-body refinement and simulated annealing as implemented in CNS. The lower completeness was responsible for difficulties in tracing the more mobile fragments of the models.

Quality of the Final Model. The resulting quality of the structure is slightly impaired by the lack of complete data. Nevertheless, the quality of the structure can be described as good as judged by the *R* factor, quality of the maps, as well as the stereochemistry of the final model. Figure 1 shows an example of the electron density at the active site of the monomer C. The final *R* factor calculated on reflections stronger than 4σ (F) was 0.215, and that calculated on all reflections was 0.218 with an R_{free} of 0.27 (*19*).

The final model contains 1568 residues and 1016 water molecules. The NAD^+ cofactor and inorganic phosphate were found at the four active sites and refined with full occupancy. We have also found and refined in subunits B and C a metal ion (putative K^+) that is directly ligated by the NAD^+ molecules in analogy to the mIPS from other species. We have labeled this "structural" metal ion 1. A postulated "catalytic" metal ion 2′ was not detected in the electron-density maps.

The model backbone as well as side-chain geometries fall fully within the acceptable range for structures at this resolution (*22*). The Ramachandran plot (*23*) indicated that 83.4% of the residues were in the most favored region, 14.8% in the allowed region, and 1.6% in the generously allowed region, with only 0.6% in the disallowed positions. Despite low completeness (74%), the quality of the electron-density maps for the bulk of the protein was fully acceptable, resulting in high map−model correlation coefficients, while for residues exposed to the solvent, especially in the dinucleotide-binding domain, it was significantly weaker. That fact limited our ability to reliably model more solvent molecules and identify uniquely additional solvent elements.

Description of the Structure of A. fulgidus mIPS and Comparison to Other mIPSs: Monomer. The archaeal mIPS enzyme forms a homotetramer (Figure 2) that is similar to the structures from other species. The monomers are organized into two distinct domains. The first is the dinucleotide-binding domain (residues 1−218 and 332−393) that can be loosely defined as having a Rossman fold. This domain is formed by a central β sheet surrounded by α helices and extended loops. A second, catalytic or tetramerization domain (residues 219−331) is mostly composed of an extensive β sheet that is exposed at the tetramerization interface and flanked with two helices at the solvent-oriented surface. There are a total of nine helices and two extensive β sheets. For comparison, the yeast enzyme has the monomers organized into three domains: (i) a dimerization domain with mainly N- and C-termini interactions creating a dimer interface, (ii) a NAD^+-binding domain having a Rossman fold, and (iii) an interfacial tetramerization domain. Thus, the archaeal mIPS exhibits significant reorganization of the monomer architecture when compared to the larger eukaryotic mIPS enzyme. The description of the secondary structure and alignments with the yeast enzyme can be found in Table 2.

The NAD^+-binding domain of *A. fulgidus* mIPS encompasses an extensive five-stranded β sheet surrounded by six α helices. The dinucleotide-binding domain contains the N-terminal 6 residues that form the first strand of the β sheet

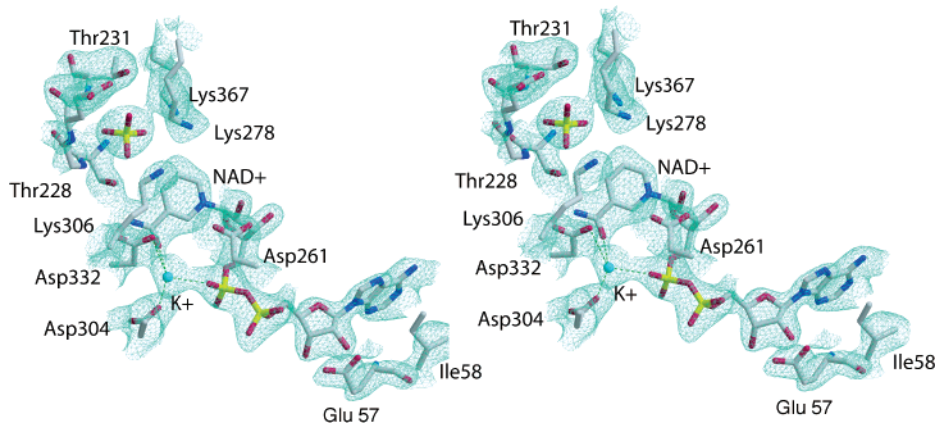

FIGURE 1: Active site of the subunit C of the refined model of *A. fulgidus* mIPS. The NAD^+ cofactor, a metal ion, and phosphate moiety are covered with the $2F_o - F_c$ electron-density map phased with the refined model contoured at a 1.1σ level.

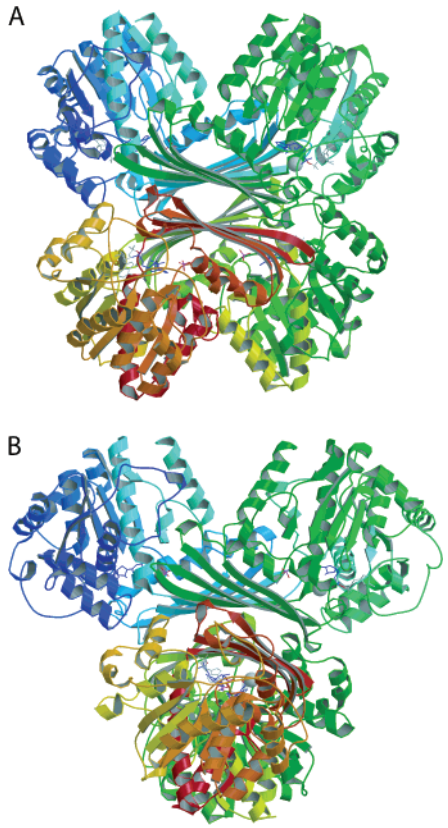

FIGURE 2: (A) Ribbon representation of the *A. fulgidus* mIPS tetramer. Note the extensive tetramer interface as well as a substantially reduced dimer interface. (B) View of the tetramer rotated by ~45°.

followed by the NAD^+-binding domain (residues 7−11). The eight helices of this domain are formed by residues 12−26, 64−75, 80−92, 124−137, 159−163, 164−174, 182−193, and 208−218. Residues 376−392 form the C-terminal helix 9.

In the initial structure of the yeast mIPS, a stretch of residues in the tetramerization domain was found unfolded in the absence of the substrate. The folding of this fragment was linked with the activation event and substrate encapsulation (10). The substrate-induced folding was suggested in the yeast mIPS to control the folding of two helices and β-sheet strand. In the *A. fulgidus* mIPS structure, the homologous stretch of residues 263−316 is folded. However, it should be remembered that (i) the archaeal mIPS is optimally active at 90 °C and at room temperature, where data were collected, this protein is likely to be more rigid than the yeast enzyme, and (ii) inorganic phosphate, a critical portion of the substrate, is bound in this site.

There is an unusual distribution of charged residues in this fragment. Helix 263−285 has a number of positively charged residues directed toward a large cavity in the interior of the protein. This cavity in the yeast enzyme has been identified as the active site (*10*). This region of *A. fulgidus* mIPS has more charged residues (5 negatively and 7 positively charged) than in the corresponding fragment of the yeast enzyme (4 negatively and 4 positively charged). The accumulation of charged residues directed toward the interior of the protein is most likely responsible for unfolding of this fragment observed in the yeast enzyme. The excess of the positive charge in *A. fulgidus* mIPS is neutralized by the negatively charged phosphate group, which is present in the archaeal protein; it is the inorganic phosphate that most likely stabilizes the folded conformation observed in the crystal structure. It is worth mentioning that the enzyme is denatured much more rapidly (and at lower temperatures) in buffers not containing inorganic phosphate (K. Neelon and M. F. Roberts, unpublished observations).

Tetramer. The archaeal mIPS homotetramer is built of a dimer of dimers (Figure 2). The dimer is formed by the hydrogen-bonded symmetric complementation of the β sheet of the tetramerization domain (residues 244−331). Residues 228−243 and 270−284 form two interfacial helices that are at the adjacent monomer interfaces and anchored to the tetramer interface.

Table 2: Comparative Mapping of Secondary Structure Elements (SSE) in *A. fulgidus* mIPS (AfIPS) Compared to *S. cerevisiae* mIPS (ScIPS) by Structural and Sequence Alignment

ScIPS	AfIPS	SSE	deletion/insertion/common[a]
1−65	none	β sheet	deletion, central domain
66−95	1−27	stand/helix	common[b]
94−103	none	strand	deletion, NAD-binding domain[c]
104−114	28−38	strand/coil/ helix	common[d]
115−129	none	strand/β turn/strand	deletion, NAD-binding domain
130−161	39−71	coil/$^3/_{10}$ helix/strand coil/helix	common
none	72−75	helix[e]	insertion, NAD-binding domain
162−206	76−120	coil/helix/coil	common
207−213	none	coil	deletion, NAD-binding domain
214−231	121−138	helix	common
232−235	none	helix	deletion
236−382	139−287	strands(4)/coil(3)/helix(4)	common
383−393	none	coil	deletion
394−460	288−354	strand(3)/coil(3)/helix(1)	common[d]
460−476	none	strand/β turn	deletion, tetramerization domain
477−518	371−392	coil(2)/helix(2)	common
518−533	none	coil/$^3/_{10}$ helix	deletion, tetramerization domain

[a] Insertions are defined as sequence segments in AfIPS that do not align with ScIPS. Deletions are defined as gaps in alignment in AfIPS relative to ScIPS. [b] This region is flanked by a β turn in ScIPS that is not in the same conformation as in AfIPS, where the region is a coil (even though the sequences align well). [c] An insertion in the Rossman fold of the ScIPS that is not present in AfIPS. [d] In *S. cerevisiae*, the coil is in a $^3/_{10}$ helix conformation. [e] This region is helical in both structures.

Table 3: Interactions of Inorganic Phosphate and NAD^+ with the Protein (Distances in Angstroms)

interaction	subunit A	B	C	D
metal ion (K^+)				
Asp304 OD2		2.78	2.88	
Nic O_1P		2.76	2.45	
Nic O_7		2.91	3.01	
Wat_1		2.86	2.73	
phosphate moiety				
O_1P				
Lys306 NZ	3.24	3.62	3.27	3.61
O_2P NZ				
Glu230 N	2.56	2.98	3.04	2.45
Gly229 N	2.62	2.68	2.77	2.67
Thr231 N	3.09	2.86	3.11	3.39
O_3P N				
Lys278 NZ	2.73	3.96	4.38	3.42
Thr231 OG1	3.10	2.84	3.26	2.84
O_4P OG1				
Lys367 NZ	3.61	2.68	2.52	3.12
NAD moiety				
adenine ring				
N_1A Tyr185 OH	3.12	3.23	2.82	2.85
N_3A Gly7 N	3.36	3.38	3.30	3.61
N_6A Thr99 O	2.69	2.50	2.64	2.68
N_6A Wat_3	3.47		3.27	
ribose sugar (adenine)				
O_2A Glu57 OE_2	3.57	3.69	2.98	2.63
O_3A Arg59 NH_2/NE	2.50	3.48	3.37	4.05
phosphate (adenine)				
O_2A Ile11 N	3.13	3.44	3.33	3.14
phosphate (nicotinamide)				
O_1P Wat_4		3.59	2.57	
O_2P Val12 N	3.13	3.05	3.23	3.33
ribose sugar (nicotinamide)				
O_3 Ala148 O	2.50	2.40	3.11	2.63
O_2 Thr150 OG1	2.90	2.90	3.03	2.33
O_3 Thr150 OG1	3.31	3.08	3.03	2.54
NAD ring				
C_5 Gly226 O	3.30	3.24	2.80	3.21
N_7 Thr228 OG1	2.78	2.76	2.66	3.68
O_7 O1phosph	3.48	4.38	4.56	3.96

The root-mean-square deviation (rmsd) between the four subunits of *A. fulgidus* mIPS (~0.49 Å on all 392 Cα) suggests that the tetramer is almost perfectly symmetric within the accuracy of the data. Nevertheless, there are numerous features of the model that suggest that the subunits are not identical. One such feature is the turn between strands three and four in the β sheet of the tetramerization domain. Subunits A and D have a type-II left-handed turn, while in subunits B and C, the same turn appears to be a type-I right-handed turn.

This asymmetry of subunits is particularly visible at the dinucleotide-binding site (the residues interacting with the NAD^+ and P_i ligands are listed in Table 3). Only two of four subunits have "structural" metal ion 1 bound at the active site. Along with the absence of metal ions in subunits A and D, there is a difference in the conformation of the NAD^+. There are also subtle differences in the NAD^+ amide nitrogen and phosphodiester oxygen when comparing NAD^+ in monomers A and D, as previously observed in the yeast mIPS structure with NADH bound.

The interfaces between the monomers are significantly altered in *A. fulgidus* mIPS compared to the yeast mIPS with looser interactions at the dimer interface and stronger at the tetramer interface (Figure 2). The loss of the N-terminal domain present in *S. cerevisiae* mIPS has separated the tightly bound monomers in the dimer, significantly weakening its interface. The tetramer interface in *A. fulgidus* mIPS is more extended with a larger contact area (Table 4). The reduced dimer interface is due mainly to deletions at the N- and C-terminal regions of the *A. fulgidus* mIPS sequence relative to yeast mIPS. An interesting feature of the tetramer interface is a symmetrical network of hydrophobic interactions that connects all four active sites (Figure 3 shows hydrophobic contacts, defined by a cutoff of 4.0 Å, across the tetramer interface). Most likely, this coupling is responsible for direct communication between the dimers, as suggested by anticooperative binding of metal ions. The analysis of quaternary interfaces, i.e., the dimerization and tetramerization interfaces, was further carried out with Dimplot (*24*). In *A. fulgidus* mIPS, the tetramer buries the surface area of 10 500 Å^2. This constitutes approximately one-third of the total surface area (33 000 Å^2) of a monomer and results in a significantly higher ratio of buried to total surface area than in the yeast structure, where 11 700 Å^2 surface area at the dimer interface and 6000 Å^2 surface area at the tetramer interface are buried. In yeast, this constitutes only 22% of the total surface area of a monomer.

A detailed analysis of the interfaces reveals differences in the types of residues directly involved in intersubunit contacts (Table 4). For both the A/B and C/D dimers, the yeast mIPS tetramer has 32 ionic and 22 hydrophobic

Table 4

Comparison of Volume, Surface Accessible Area (SAA), and Number of Interfacial Solvent Accessible Residues (SAR) for *S. cerevisiae* and *A. fulgidus* mIPS Enzymes

	S. cerevisiae		*A. fulgidus*	
volume (Å^3)[a]	188 942		157 950	
total SAA (Å^2)[a]	72 310 (0.507)[b]		73 222 (0.673)[b]	
hydrophobic SAA (Å^2)[c]	18 362		14 400	
polar SAA (Å^2)[c]	21 851		17 329	
charged SAA (Å^2)	32 097		41 493	
	tetramer	dimer	tetramer	dimer
analysis by residues[c]				
hydrophobic (SAR)	144	94	120	38
polar (SAR)	128	80	116	16
charged (SAR)	127	76	108	30

Comparison of the Buried Area and Number of Interfacial Solvent Inaccessible Residues for *S. cerevisiae* and *A. fulgidus* mIPS Enzymes[d]

	S. cerevisiae		*A. fulgidus*	
	tetramer	dimer	tetramer	dimer
buried area at interfaces (Å^2)[e]	5686	11 301	10 500	4960
number of residues buried[f]				
hydrophobic	24	30	56	26
polar	36	14	40	10
ionic	128	4	8	2

[a] Calculations were performed with GRASP. [b] Fraction of the buried solvent accessible area to the total solvent accessible area. [c] Calculations are based on PDB generated with surface_plot.inp in CNS, and interfaces are reported as tetramer and averaged dimer interfaces. [d] Interfacial interactions identified by Dimplot and are reported as AB/CD. [e] Calculations for the buried surface area at interface are based on GRASP. [f] Calculations done for residue numbers and the buried surface area are based on output from CNS buried_surface.inp. Dimer interfaces are averaged AB and CD.

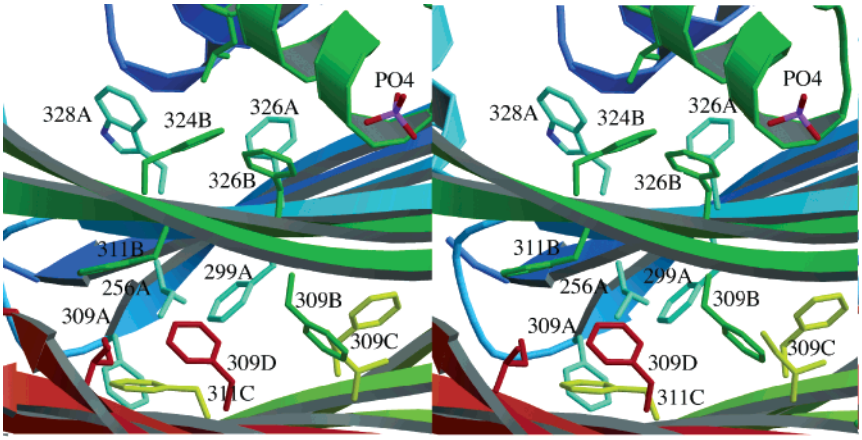

FIGURE 3: Close-up view of the tetramer interface focused on the hydrophobic contacts at the dimer−dimer interface.

contacts at the tetramer interface and 36 ionic and 44 hydrophobic contacts at the dimer interface. In contrast, *A. fulgidus* mIPS has a total of 36 ionic and 16 hydrophobic contacts at the dimer interface and 42 ionic and 132 hydrophobic contacts at the tetramer interface. The *M. tuberculosis* mIPS has 22 ionic and 12 hydrophobic contacts at the dimer interface and 32 ionic and 64 hydrophobic contacts at the tetramer interface. The archaeal mIPS has a dimer interface similar to that of *M. tuberculosis* mIPS. Both proteins have shorter primary sequences than yeast mIPS that results in diminished dimeric interactions as described above. Therefore, the most important interface in those two mIPS molecules is the tetramer interface.

Comparison of Available mIPS Structures. To gain additional insights into the conservation patterns between sequences of the proteins representing different kingdoms, we carried out primary sequence alignment for the mIPS from two *Pyrococcus* species, *Thermotoga maritima*, *Arabidopsis thaliana*, human, and *Pichia pastoris*, as well as *A. fulgidus* and *S. cerevisiae*. The shorter bacterial species clustered together with characteristics distinct from eukaryotic sequences. The number and the conservation pattern for the charged residues was distinctly different for the archaeal and eukaryotic sequences. Other motifs have been noted and described previously (*10*).

A structural superimposition of *A. fulgidus* mIPS on *S. cerevisiae* or *M. tuberculosis* mIPS is shown in parts A and B of Figure 4 along with the resulting sequence alignment (Figure 5). Superimposing the core residues resulted in 329 structural equivalents with an rmsd of 1.69 Å; superposition with 382 total matches resulted in an rmsd of 2.32 Å. There were a number of major deletions compared to the yeast structure (summarized in Table 2). One of the prominent deletions was the loss of 160 residues of yeast sequence from both the N and C terminus that contribute to the dimer interface. This deletion is responsible for the reduced dimer interface of the *A. fulgidus* mIPS. Another large deletion occurred within the NAD^+-binding domain. In *A. fulgidus* mIPS, part of an insert to the dinucleotide-binding domain corresponding to yeast residues 90−103 was missing. The two major insertions in *A. fulgidus* mIPS compared to *M. tuberculosis* are shown in Figure 4B and are detailed below.

A direct correspondence between the active-site residues in *A. fulgidus* mIPS and residues in the yeast structure (in parentheses) was found: Thr228(Ser323), Gly229(Gly324), Thr230(Thr326), Asp261(Asp356), Lys274(Lys369), Lys278-

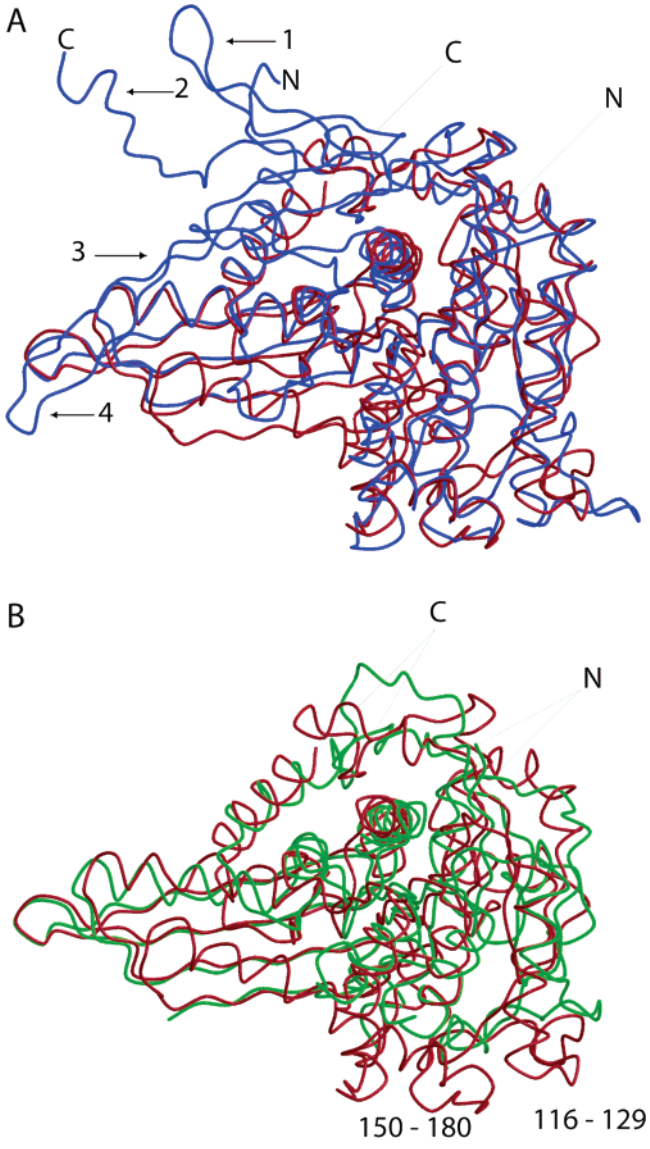

FIGURE 4: Superimposition of *A. fulgidus* mIPS monomer (in red) on (A) *S. cerevisiae* monomer (in blue) and (B) *M. tuberculosis* monomer (in green). Note the major structural deletions in *A. fulgidus* mIPS compared to the yeast enzyme.

```
AF ------------------------------------------------------------ 0
SC itsvkvvtdkctykdnelltkysyenavvtktasgrfdvtptvqdyvfkldlkkpek 65
MT ----------------------------------------MSEHQSLPAPEASte 15

AF MKVWLVGAYGIVSTTAMVGARAIERGI----------A--PKIGLVSEL-------- 37
SC LGIMLIGLGGNNGSTLVASVLANKHNVefqtkegvkqP--NYFGSMTQCstlklgid 120
MT VRVAIVG-VGNCASSLVQGVEYYYnad----------dtstVPGLMH---------- 51

AF --------PHFEgieKYAPF-SFEF-GGHEIRLL---sNAYEAAKEHwelnrHFDRE 81
SC aegndvyaPFNSll-PMVSPnDFVV-SGWDINNA----DLYEAMQRS----qVLEYD 167
MT -----------vrfgpyhvR-DVKFvAAFDVDAKkvgFDLSDAIFAsenntikiad- 95

AF ILEAVKSDLEGIVARKGTAL--nc-gSGIK-ELgdiktle-----geglSLAEMVSR 129
SC LQQRLKAKMSLVKPLPSIYYpdfi-aANQD-ERanncinldekgnvttrGKWTHLQR 222
MT ----VAPT--NVIVQRGPTL--DGiGKYYAdtielsdae---------------pvD 129

AF IEEDIKSFA----DDETVVINVASTEPLPNYSEEYHGSLEGFERMIDEDRkEYASAS 182
SC IRRDIQNFKeenaLDKVIVLWTANTERYVEVSPGVNDTMENLLQSIKNDH-EEIAPS 278
MT VVQALKEAK----vd--VLVSTLPVGse--------------------------EAD 154

AF MLYAYAALKLGLPYANFTPSPGSaIPALKELAEKKGVPHAGNDGKT--GETLVKTTL 237
SC TIFAAASILEGVPYINGSPQNTF-VPGLVQLAEHEGTFIAGDDLKS--GQTKLKSVL 332
MT KFYAQCAIDAGVAFVNALPVFIAsDPVWAKKFTDARVPIVGDDIKSqvGATITHRVL 211

AF APMFAYRNMEVVGWMSYNILGDYDGKVLSARDNKESKVLSKdKVLEKMLG------- 287
SC AQFLVDAGIKPVSIASYNHLGNNDGYNLSAPKQFRSKEISKsSVIDDIIAsndily- 388
MT AKLFEDRGVQLDRTMQLNVGGNMDFLNMLERERLESKKISKTQAVTSNLKr------ 262

AF -----ySPYSITEI-QYFPSLVDNKTAFDFVHFKGFLGKLMKFYFIWDAIDAIVAAP 338
SC ndklgkKVDHCIVI-KYMKPVGDSKVAMDEYYSELMLGGHNRISIHNVCEDSLLATP 444
MT ---efKTKDVHIGPsDHVGWLDDRKWAYVRLEGRAFGDVPLNLEYKLEVWDSPNSAG 316

AF LILDIARFLLFAKKKG----------------vkGVVKEM-AFFFKSPM----dtNV 374
SC LIIDLLVMTEFCTRVSykkvdpvkedagkfenfyPVLTFL-SYWLKAPLtrpgfhPV 500
MT VIIDAVRAAKIAKDrg----------------IGGPVIPAsAYLMKSPP----EqlP 353

AF INTHEQFVVLKEWYSNlk--------------- 392
SC NGLNKQRTALENFLRLliglpsqnelrfeerll 533
MT -----DDIARAQLEEfiig-------------- 367
```

KEY:
Identity
Homologous classified as: polar, charged or hydrophobic
Substitution in crucial active site residues
Conserved active site and phosphate binding site residues
MT residues missing in unliganded crystal structure.
Lower case indicates insertion or lack of sequence identity or homology.

FIGURE 5: Structural sequence alignment done in Sequoia using the available three-dimensional structures of *A. fulgidus*, *M. tuberculosis*, and *S. cerevisiae* mIPS enzymes. Identical residues are in red; homologous residues, in blue; and active-site residues, in green. The residues not present in the crystal structures are highlighted in orange.

(Lys373), Lys306(Lys412), Asp332(Asp356), and Lys367-(Lys489). Most of those residues are conserved, while others are highly homologous.

Additionally, the comparison indicated several residues, such as Asp259 in the *A. fulgidus* mIPS sequence, that are distinct for archaeal, bacterial, or eukaryotic mIPS enzymes. The number of positively and negatively charged residues found in the vicinity of the active site in the archaeal enzyme was also different from what was observed in the yeast enzyme. For example, Asp259 in *A. fulgidus* mIPS corresponds to position 354 in the yeast enzyme where it is Asn. Asp259 is located at the beginning of a short helix leading to the crucial 267−287 helix that was found unwound in the absence of the substrate in yeast mIPS. The electrostatic field at the active site is also influenced by the presence of numerous negatively charged residues in the first domain.

A series of glutamate residues (Glu24, Glu36, Glu41, Glu44, and Glu52) in the vicinity of the active-site cavity of the archaeal mIPS do not have corresponding acidic residues in other species.

Several mIPS have higher sequence homology both at the N-terminal region and around residue 150. This region constitutes a solvent-accessible loop that is conserved in yeast and *A. fulgidus* enzymes but not the *M. tuberculosis* mIPS (see Figure 4). This highly charged and solvent-accessible loop has a significant influence on the solubility in the mIPS from *Pyrococcus abyssii* (*25*).

A number of aspartate and lysine residues in *M. tuberculosis* mIPS had counterparts in the *A. fulgidus* mIPS. These include Asp261(Asp220), Asp304(Asp241), Lys227(Lys186), and Lys306(Lys243) where the *M. tuberculosis* mIPS residue is shown in parentheses. There were three interesting features in the archaeal mIPS that did not occur in the bacterial mIPS. (i) A gap in the *A. fulgidus* mIPS occurred where the bacterial mIPS has an insertion in the Rossman motif. (ii) A large inserted sequence in the archaeal mIPS (residues 116−129) corresponds to a loop in the yeast mIPS structure that is conserved among several eukaryotic mIPS sequences. (iii) A solvent-accessible region of the dinucleotide-binding domain from residues 150 to 180 that is involved in crystal contacts is only present in the archaeal enzyme. This region of the dinucleotide-binding domain that is poorly conserved in other bacterial mIPS may aid in conformational changes necessary during substrate binding. Particularly, residues 148−150 come into direct hydrogen-bonded contact with NAD^+. Additionally, residues 152−154 and 201−203 that are in direct van der Waals contact in neighboring strands contain the sequence Pro-X-Pro that usually is associated with structural strain. As a result, residues 155−158 have higher than average temperature factors and appear to be partially disordered. All those above-mentioned residues are also structural neighbors of the interfacial helix 267−287 that was found unwound in the yeast enzyme.

Phosphate and Metal-Ion Binding in the Active Site. The clustering of negative and positive residues gives rise to a highly polarized and charged active site in *A. fulgidus* mIPS. The cluster of negatively charged amino acids is important for the metal-ion binding and the cluster of the positive amino acids for coordination of the phosphate group of substrate G-6-P. In Figure 6, the NAD^+-binding pocket is depicted with "structural metal ion 1". Details of residues that coordinate NAD^+ are in Table 3. NAD^+ interacts directly with several residues at the active site. Ser149 is in close enough proximity to interact with the NAD^+ pyrophosphate oxygens, and Asp261 is only 2.63 Å from nicotinamide ribose hydroxyls. Ile11 contributes a backbone interaction stabilizing the adenine portion of the NAD^+ moiety. The difference electron-density maps suggested that a tetrahedral moiety was bound at the opposite site of the NAD^+-binding pocket. The omit difference electron-density maps confirmed the presence of an inorganic phosphate anion bound at the N-terminal end of second interfacial α helix of the tetramerization domain (243−257), a typical motif for phosphate-group binding (*26*). Stabilization by the dipole moment of an α helix is the most common motif used for binding phosphate groups, and, in fact, two helices of the dinucleotide binding domain are directed toward the pyrophosphate group of NAD^+.

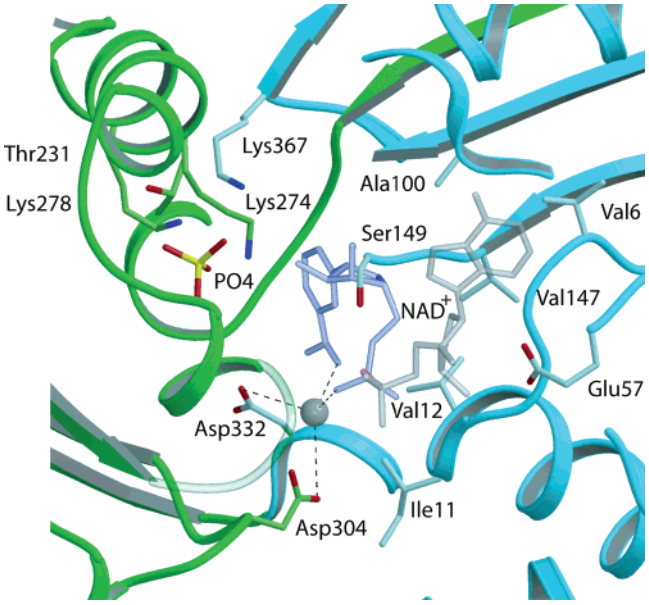

FIGURE 6: General view of the *A. fulgidus* mIPS active site of monomer C showing K^+, inorganic phosphate, and NAD^+. The metal ion is shown coordinating NAD^+ (bonds in broken lines) as well as residues Asp332 and Asp304.

In the direct vicinity of the NAD^+, a large peak was found in the difference electron-density map that was subsequently modeled as a metal ion. Possible candidates for this metal ion included the activating metals Mn^{2+}, Mg^{2+}, and Zn^{2+}, as well as monovalent cations such as Na^+ or K^+. The final step in the purification of this mIPS involved dialyzing the protein against EDTA, a step that led to low enzyme activity unless the assay mix was supplemented with Zn^{2+}, Mn^{2+}, or Mg^{2+} (*6*). However, *A. fulgidus* has high (∼1 M) concentrations of intracellular K^+ (*27*), and binding of K^+ could be critical to the structure and function of many *A. fulgidus* enzymes. The identity of the crystallographically observed metal ion was assigned by careful examination of resulting *B* factors, map quality, and finally the expected coordination obtained from refinements with different metal ions. The coordination number (4 or 5) as well as the distances to protein side chains and water ligands in the range of ∼2.4−3.0 Å seemed to be consistent with potassium ions. The refinement confirmed the identity of K^+ ions in both monomer B and C sites, with occupancy refining to 100% and comparable temperature factors with that of the surrounding atoms. The cation in monomer B (and C) is coordinated by the NAD^+ phosphate, nicotinamide O7, Asp304, and water 1602 in a distorted tetrahedron that would be acceptable for K^+. It cannot be excluded that monovalent cations compete with divalent cations for coordination at this metal-ion/NAD^+-binding site.

Detailed refinement of models for yeast and *M. tuberculosis* mIPS enzymes revealed metal ions in these crystal structures. In the yeast enzyme (*12*, *13*), the distances from the amide carbonyl of the nicotinamide ring as well as phosphate oxygens of NAD^+ to the metal ion were around 2.0 Å, suggesting that the bound ion was a divalent metal ion such as Mg^{2+} or Zn^{2+}. Furthermore, EDTA treatment removed the metal ion from the enzyme. Reduction of NAD^+ to NADH in the yeast enzyme appeared to influence the affinity of the protein for the metal ion. In *M. tuberculosis* mIPS, the tetrahedral coordination suggested a bound Zn^{2+},

but the refinement resulted in 50% occupancy. The conformation of cofactor NAD^+ is likely to be critical for the enzymatic reaction. If, indeed, the tetramer exhibits negative cooperativity and only half of the subunits have filled metal-binding sites, the applied symmetry to the *M. tuberculosis* mIPS structure would indeed produce 50% occupancy. The flexibility of NAD^+ and NADH in this region could allow the cofactor to exist in different forms, thus controlling catalysis.

In the *A. fulgidus* mIPS structure, the distances between the NAD^+ carbonyl amide moiety of the nicotinamide ring and the NAD^+ phosphate oxygens vary in the different subunits (Table 3). Differences between the four NAD^+ molecules in the *A. fulgidus* monomers clearly correlated with the presence of a metal in a particular subunit. Distances were longer in subunits with K^+ (~4.4 Å) than in the subunits without metal ion (~3.9 Å). In all of the subunits, these distances were longer than required for a direct hydrogen-bond distance between the amide and the phosphate moiety. The rmsd between the NAD^+ molecules in the different subunits of *A. fulgidus* mIPS showed comparable variation to that seen in bacterial and yeast mIPS structures.

On the other side of the nicotinamide ring, there is a charge-coupled system of Asp225 and Lys367. In three subunits, the carboxyl group of Asp225 is in hydrogen-bonding distance to C6 of the nicotinamide ring. The C4, C5, and C6 carbon atoms are involved in direct interactions with acceptor groups such as Thr228, carbonyl of Gly226 and the headgroup of Asp225, respectively. This suggests that these residues are critical to catalysis and are involved in strict control of protonation of NAD^+. In fact, Lys367 amino group hydrogen bonds to both the carbonyl of Ser266 and Asp225.

Thermostability of A. fulgidus mIPS. A. fulgidus mIPS has previously been shown to be very thermostable (*6*) with an optimal specific activity of ~90 °C (short-time single-concentration assays). In contrast, the yeast mIPS exhibited thermal stability only up to ~55 °C (Figure 7A). The half-life for the loss of activity by the *A. fulgidus* mIPS at 98 °C in 50 mM Tris-HCl at pH 8.0 was ~40 min (Figure 7B). Although maximal specific activity was detected at 55 °C for the yeast enzyme, in the absence of added substrate or cofactor, the enzyme quickly lost activity ($t_{1/2} \sim 5$ min) when incubated in 50 mM Tris-HCl at pH 8.0 and 55 °C (Figure 7B). The cofactor NAD^+ alone at 1 mM did not provide any protection from heat inactivation, while 5 mM G-6-P in the incubation mixture helped to stabilize the enzyme (Figure 7B).

There are several structural features that can be implicated in the significantly greater thermostability of the archaeal enzyme. The analysis of amino acid content shows an increased amount of Ile and Lys residues and much lower content of Asn, Gln, and Ser residues, changes consistent with trends observed for other thermostable enzymes (*28*). The most interesting observation is the pattern of charged residues that stabilize a number of the turns in the *A. fulgidus* mIPS structure. Shortening of external loops has been suggested to enhance protein thermostability (*29*), and many external loops in *A. fulgidus* mIPS are indeed shortened or deleted relative to yeast mIPS (see Figure 4A). Examples of complete elimination or significant shortening of the loops include several in the dinucleotide binding domain (Table 2). The last loop is an especially interesting case in which a short deletion is accompanied by introduction of an aspartate (Asp139 in *A. fulgidus*) that directly stabilizes the turn by internal hydrogen bonding to the backbone atoms at the turn.

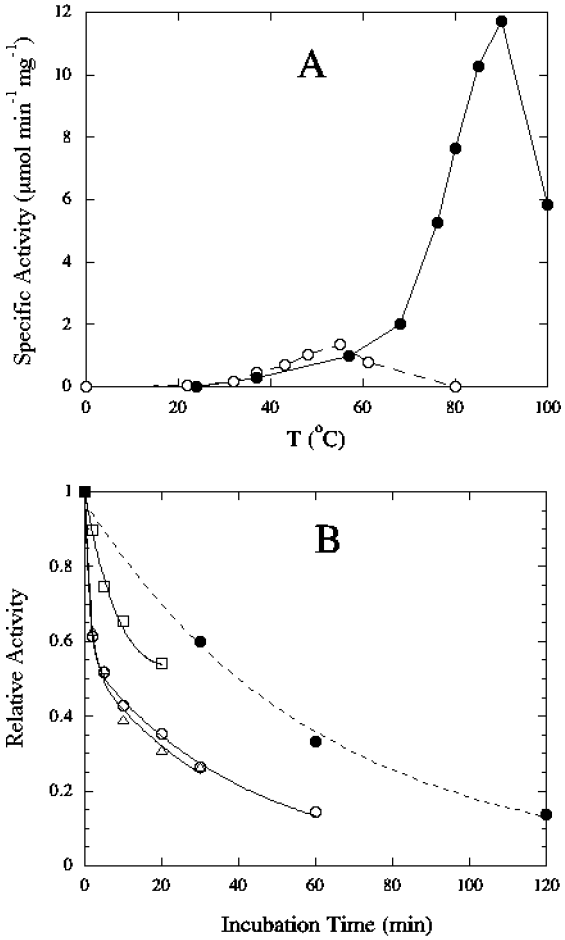

FIGURE 7: (A) Temperature dependence of mIPS activity. (●) *A. fulgidus* mIPS (3 min assays; data from ref *6*). (○) *S. cerevisiae* mIPS (7 min assays). (B) Thermal stability of (●) *A. fulgidus* mIPS preincubated at 98 °C and *S. cerevisiae* mIPS preincubated at 55 °C in the absence (□) and presence of 1 mM NAD^+ (○) or 5 mM G-6-P (△).

The increased ratio of buried to total surface area may also contribute to the much higher thermal stability of the *A. fulgidus* mIPS (*6*). An example of these buried interfacial interactions (Figure 3) include the hydrophobic triad Trp328 and Phe326 from monomer B interacting with Phe324 in monomer A. Complementary interactions occur in subunit A, where Trp328 and Phe326 are interacting with monomer B Phe324.

Mechanistic Aspects of the Structure: Electrostatics Suggest a Second Metal-Ion-Binding Site in A. fulgidus mIPS. The occupancy of metal ions and possible competition between mono- and divalent cations brings into question the role of metal ions in catalysis (*6*). In the absence of added metal ions to the recombinant *A. fulgidus* mIPS, the specific activity was 20−30% of the maximum activity. That observation could be consistent with partial occupancy of a metal ion near the NAD^+ molecule. However, it cannot be K^+, because there is a change in the catalytic rate in the presence of EDTA. The first step of the reaction that transforms G-6-P into 5-keto-G-6-P has an initial rate at 85 °C much slower (0.0017 s^{-1}) in the presence of EDTA than

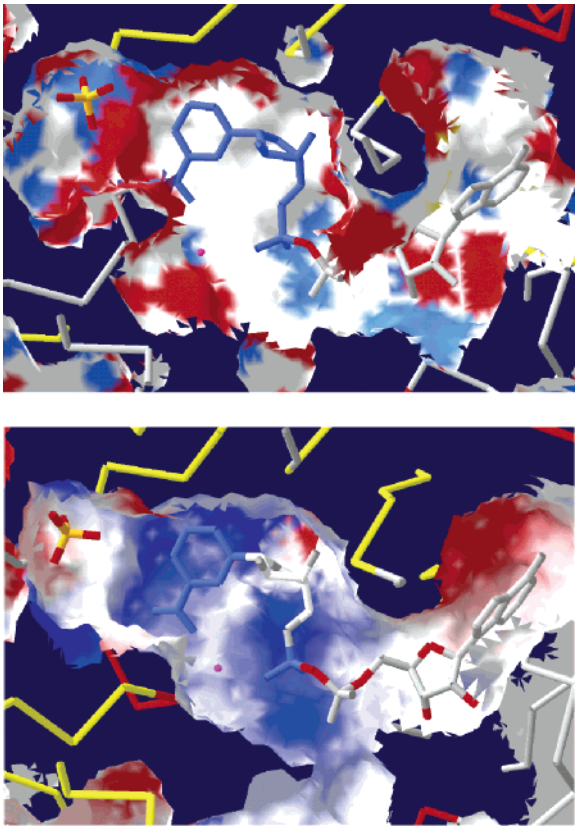

FIGURE 8: Comparison of electrostatic surface images of archaeal and yeast mIPS active sites. (A) *A. fulgidus* mIPS (upper panel). (B) *S. cerevisiae* mIPS (lower panel). Please note the much more negatively charged (less blue and more red) *A. fulgidus* mIPS active site.

in its absence ($k_{cat} \sim 8\ s^{-1}$). This indicates that the first step, as well as the cyclization, is kinetically impaired in the presence of EDTA. Additionally, NADH production appeared biphasic with EDTA present (*6*). Finally, the production of I-1-P is prevented unless Zn^{2+}, Mn^{2+}, or Mg^{2+} are provided. All of these data suggested that there should be a second metal-ion site in the archaeal mIPS.

The metal ions observed crystallographically in the *A. fulgidus* mIPS appear to have limited contact with the substrate, hence their influence cannot explain the experimental results described above. Furthermore, K^+ will not be chelated by the EDTA, so that it cannot be the ion whose loss is reflected in the slow first step of I-1-P formation with EDTA present. Modeling of the active-site electrostatic environment of both yeast and *A. fulgidus* mIPS was undertaken to obtain insights into other possible binding sites for divalent cations that would be unique to the archaeal enzyme. The electrostatic field was calculated for these two structures in GRASP after all ligands were removed. The surrounding of the active sites in both enzymes are visualized in Figure 8.

As seen in Figure 8A, the *A. fulgidus* mIPS active site clearly exhibits a strong anionic pocket where the conserved Asp residues are located. The electrostatic potential is much more negative than that present in the yeast enzyme. Numerous negatively charged residues not necessarily directly located at the active site contribute to this potential. For example, the previously discussed glutamate residues located at the N-terminal region that are conserved among

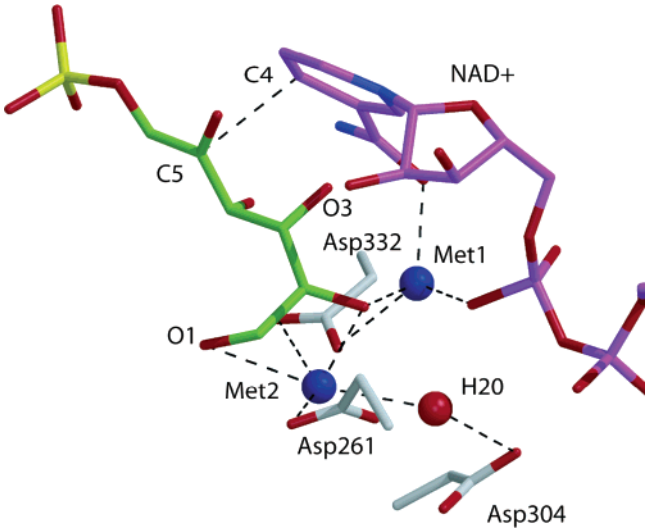

FIGURE 9: Model of linearized G-6-P (green, with NAD^+ in purple) docked in the active site of *A. fulgidus* mIPS showing C4, C5, and phosphate of G-6-P. Two metal ions are positioned as described in the text.

bacterial species contribute to this field. This highly negative electrostatic potential suggests that more than one metal may be coordinated in the presence of NAD^+ and G-6-P at the active site.

In *S. cerevisiae* mIPS, the aspartate residues conserved with *A. fulgidus* mIPS (in parentheses), Asp410(Asp304) and Asp438(Asp332), show much less contribution to the anionic electrostatic potential than their archaeal counterparts. This may be due in part to positioning of crucial Lys residues. For example, the mobile Lys412 side chain points inward and is located ~4.2 Å from Asp438 and Asp410 and is only 3.78 Å from Lys439. What seems to be most important is that the active-site negative charge is dissipated by the loss of the negative charge, with Asn354 in *S. cerevisiae* replacing Asp259 residue in *A. fulgidus*. The adjacent Asn355 and Ans354 side chains in yeast mIPS and nearby Arg160 and Arg198 shield the active site from divalent cations leaving Asp356 as an isolated negative charge. The net result of these changes is that the yeast active site does not have an anionic pocket formed near the cofactor and substrate.

Modeling of Substrate/Reaction Intermediates and Activating Metals in the Active Site of A. fulgidus mIPS. The calculated electrostatic potentials for *A. fulgidus* mIPS led us to model substrates or the first reaction intermediate in the active site in the presence of the cofactor and activating metal ions. The phosphate group of G-6-P was superimposed on the inorganic phosphate found in the crystal structure, and the extended carbon chain of linearized sugar was extended toward the NAD^+ molecule reaching to the metal-binding site. Only the linearized form of glucose could be docked at this site; the cyclic form of G-6-P collided with surrounding residues. The C5 hydroxyl of G-6-P was oriented toward the NAD^+, suggesting a direct proton transfer. Before energy optimization of the protein with G-6-P docked, a Zn^{2+} ion was modeled into the site of the crystallographic potassium ion. During energy optimization with linearized G-6-P present, the ion moved <1 Å.

Subsequently, the acyclic 5-keto-G-6-P intermediate was modeled in the presence of NADH and inclusion of two activating Zn^{2+} metals. As shown in Figure 9, the "structural"

metal ion 1 was close to the putative Mg^{2+} in the yeast NADH-bound structure (*13*). Its role is likely to correctly orient the NAD^+/NADH and induce necessary polarization in it to prepare for the first protonation step. The second metal-ion site of the *A. fulgidus* mIPS is close to a putative NH_4^+-binding site of the yeast enzyme (*13*). A second Zn^{2+} ion, the "catalytic" metal ion, had an optimal position near substrate O1 and had ligands coming from the NAD^+, a water molecule, Asp304 in direct coordination sphere, and possibly Asp332. The polarization imposed by this second cation is likely to be important for ring closure and direction proposed by Geiger et al. (*13*). The location of the second metal ion varied depending on whether G-6-P or an intermediate was included in the energy minimization. Such a location agrees with the changeable position for the second metal ion found in xylose isomerase (*30*).

The modeling also highlights several other residues that appear critical for binding of the substrate and cofactor NAD^+. Lys274 appears to be a key residue in the stabilization of O5 during enolization, being located only 3.68 Å from the NAD^+. Leu257 is coplanar with the closed ring of the product and could help to stabilize binding of inositol or glucose moieties. Lys306 may work in concert with Asp332 and aid in positioning the acidic residue so that it can interact with a metal ion.

Catalytic Mechanism for mIPS. On the basis of modeling of substrates and intermediates at the active site for both the archaeal and yeast enzymes, we can propose a mechanism for *A. fulgidus* mIPS that is highly confluent with current views on yeast mIPS. Certain characteristics of both enzymes are the same, and they allow us to draw clear parallels between both reactions. The presence of the multiple-conserved lysine residues, the NAD^+, and a crystallographically observed metal ion create a reference frame for the catalytic events.

The reaction commences when the proton is lost from the C5 hydroxyl of G-6-P. It is most likely transferred to Lys274 (Lys369 in yeast). Asp225 (Asp320 in yeast), positioned nearby, could accept the proton in a relay fashion as characterized before in the yeast enzyme. This deprotonation makes the oxidation of G-6-P at the C5 position relatively easy because the reactive C4 of the nicotinamide ring of NAD^+ is positioned for a direct hydride transfer. The creation of a ketone at position C5 allows for some conformational rearrangements and subsequent enolization at the C5−C6 bond. For the enolization step to occur, Lys367 or Lys489 in yeast acts as a base withdrawing a *pro*-R proton from the C6. A proton-withdrawing role of the phosphate group in this step may also need to be considered. According to this model, the developing negative charge on the enolate oxygen would be stabilized in the archaeal enzyme by Lys274 and Lys367.

All of those steps as well as the subsequent aldol condensation require significant suppression of the pK_a of the participating amino groups of four crucial lysine residues (274, 278, 306, and 367) at some point during the reaction. The role of those charged residues was clearly demonstrated by the mutagenesis experiments reported by Geiger's group (*13*). The much smaller but more negatively charged archaeal enzyme may not offer a positive enough electrostatic environment for the subsequent step to progress. This would be provided by an additional divalent cation.

The aldol condensation/cyclization step can occur only after a large conformational change that brings the C1 closer to the C6 and the phosphate group (*13*). The archaeal mIPS is proposed to use the second metal ion to provide the necessary stabilization of the negative charge on O1. Additional stabilization comes from lysine residues in the vicinity (Lys306 and Lys278, both close to the O1). One or both can also contribute to the final OH regeneration at this position.

The last step is the reduction of the inosose compound by NADH. In this step, a direct hydride transfer would protonate C5. The results of our modeling support numerous biochemical reports that there should be a retention of configuration at this position. The charge relay system of Asp225 and Lys367 might help to regenerate a hydroxyl group at this position.

CONCLUSIONS

Using X-ray crystallographic techniques, we have determined the structure of the first archaeal mIPS. The structure is similar in ternary as well as quaternary organization to the eukaryotic mIPS, despite the smaller size of the subunits (44 versus 60 kDa). Factors contributing to thermostability of the archaeal mIPS include shortened mobile loops relative to both eukaryotic species and an interlocking network of hydrophobic residues at the tetramer interface. Its similarity to the mIPS from *M. tuberculosis* underlines common structural motifs across life kingdoms and suggests that the evolutionary origins of this protein are not so ancient.

The *A. fulgidus* mIPS crystallized with each subunit containing inorganic phosphate and two of the four containing a monovalent metal ion most likely to be K^+. The differences in NAD^+ conformation in sites with K^+ versus those sites without the ion suggest that the enzyme may exhibit negative cooperativity in its activity. Indeed, this can be seen in NADH formation when the enzyme is incubated with G-6-P and NAD^+ in the presence of EDTA (*6*).

The presence of a metal ion and inorganic phosphate suggested a unique mode of modeling the substrate at the active site. Although details of the mechanism require further work, there are common mechanistic elements for mIPS from eukaryotic, bacterial, and archaeal organisms. The substrate phosphate group occupies a very similar position in each of the mIPS structures. A single metal ion is bound to the carbonyl moiety of the nicotinamide ring and provides polarization necessary for the first proton-transfer step of the reaction. The presence of a monovalent metal ion is consistent with difficulties in its identification in eukaryotic species and resistance to EDTA.

Divergence in the mechanism between the archaeal and eukaryotic mIPS occurs with the use of a second metal ion. In the archaeal enzyme, it is used to stabilize the transition state of the cyclization step by interacting with the oxygen on C1. In the eukaryotic enzyme, this role is most likely served by the monovalent activator NH_4^+. Thus, we suggest a two-metal-ion mechanism for the archaeal mIPS: one metal ion is critical for proper positioning of NAD^+ and substrate, and the other metal is critical for stabilization of the negative charge on O1 during the aldol condensation (cyclization).

An element that is common to all mIPS enzymes is the participation of numerous lysine residues at the positively

charged corner of the active site. We postulate that either Lys306 or Lys274 participates directly in cyclization in *A. fulgidus* mIPS. Single-site mutants of the archaeal protein should test the details of the proposed catalytic mechanism.

ACKNOWLEDGMENT

We thank Dr. J. H. Geiger for providing the coordinates of *S. cerevisiae* mIPS synthase before publication and for helpful discussions.

REFERENCES

1. Overduin, M., Cheever, M. L., Kutateladze, T. G. (2001) Signaling with phosphoinositides: Better than binary, *Mol. Interventions 1*, 150−159.
2. Clark, G. B., Thompson, G., Jr., and Roux, S. J. (2001) Signal transduction mechanisms in plants: An overview, *Curr. Sci. 80*, 170−177.
3. Fahey, R. C. (2001) Novel thiols of prokaryotes, *Annu. Rev. Microbiol. 55*, 333−356.
4. Roberts, M. F. (2004) Osmoadaptation and osmoregulation in archaea, *Front. Biosci. 9*, 1999−2019.
5. Majumder, A. L., Johnson, M. D., and Henry, S. A. (1997) 1-L-*myo*-Inositol-1-phosphate synthase, *Biochim. Biophys. Acta 1348*, 245−256.
6. Chen, L., Zhou, C., Yang, H., and Roberts, M. F. (2000) Inositol-1-phosphate synthase from *Archaeoglobus fulgidus* is a class II aldolase, *Biochemistry 39*, 12415−12423.
7. Tian, F., Migaud, M. E., and Frost, J. W. (1999) *myo*-Inositol-1-phosphate synthase: Does a single active-site amino acid catalyze multiple proton transfers? *J. Am. Chem. Soc. 121*, 5795−5796.
8. Loewus, M. W., and Loewus, F. (1973) Characterization of *myo*-inositol-1-phosphate synthase from *Acer pseudoplatanus*, *Plant Sci. Lett. 1*, 368−371.
9. Mauck, L. A., Wong, Y. H., and Sherman, W. R. (1980) L-*myo*-Inositol-1-phosphate synthase from bovine testis: Purification to homogeneity and partial characterization, *Biochemistry 19*, 3623−3629.
10. Stein, A. J., and Geiger, J. H. (2002) The crystal structure and mechanism of 1-L-*myo*-inositol-1-phosphate synthase, *J. Biol. Chem. 277*, 9484−9491.
11. Norman, R. A., McAlister, M. S., Murray-Rust, J., Movahedzadeh, F., Stoker, N. G., and McDonald, N. Q. (2002) Crystal structure of inositol 1-phosphate synthase from *Mycobacterium tuberculosis*, a key enzyme in phosphatidylinositol synthesis, *Structure 10*, 393−402.
12. Jin, X., and Geiger, J. H. (2003) Structures of NAD^+- and NADH-bound 1-L-*myo*-inositol-1-phosphate synthase, *Acta Crystallogr., Sect. D 59*, 1154−1164.
13. Jin, X., Foley, K. M., and Geiger, J. H. (2004) The structure of the 1-L-*myo*-inositol-1-phosphate synthase−NAD^+−2-deoxy-D-glucitol 6-(*E*)-vinylhomophosphonate complex demands a revision of the enzyme mechanism, *J. Biol. Chem. 279*, 13889−13895.
14. Lowry, O. H., Rosebrough, N. J., Farr, A. L., and Randall, R. J. (1951) Protein measurement with the folin phenol reagent, *J. Biol. Chem. 193*, 265−275.
15. Jankarik, J., and Kim, S. H. (1991) Sparse matrix sampling: A screening method for crystallization of proteins, *J. Appl. Crystallogr. 24*, 409−411.
16. Brunger, A. T. (1992) *X-PLOR, Version 2. 1. A System for Crystallography and NMR*, Yale University Press, New Haven, CT.
17. Kniewel, R., Buglino, J. A., Shen, V., Chadha, T., Beckwidth, A., Lima, C. D. (2002) Structural analysis of *Saccharomyces cerevisiae myo*-inositol phosphate synthase, *J. Struct. Funct. Genomics 2*, 129−134.
18. Brunger, A. T., Krukowski, A., and Erickson, J. (1990) Slow-cooling protocols for crystallographic refinement by simulated annealing, *Acta Crystallogr., Sect. A 46*, 585−593.
19. Sheldrick, G. M., and Schneider, T. R. (1997) SHELXL: High-resolution refinement, *Methods Enzymol. 277*, 319−343.
20. McRee, D. E. (1999) XtalView/Xfit−A versatile program for manipulating atomic coordinates and electron density, *J. Struct. Biol. 125*, 156−165.
21. Bruns, C. M., Hubatsch, I., Ridderström, M., Mannervik, B., and Tainer, J. A. (1999) Human glutathione transferase A4-4 crystal structures and mutagenesis reveal the basis of high catalytic efficiency with toxic lipid peroxidation products, *J. Mol. Biol. 288*, 427−439.
22. Engh, A. A., and Huber, R. (1991) Accurate bond and angle parameters for X-ray protein structure refinement, *Acta Crystallogr., Sect. A 47*, 392−400.
23. Ramachandran, G. N., Ramakrishnan, C., and Sasisekharan, V. (1963) Stereochemistry of polypeptide chain configurations, *J. Mol. Biol. 7*, 95−99.
24. Wallace, A. C., Laskowski, R. A. and Thornton, J. M. (1995) LIGPLOT: A program to generate schematic diagrams of protein−ligand interactions, *Protein Eng. 8*, 127−134.
25. Vieille, C., and Zeikus, G. J. (2001) Hyperthermophilic enzymes: Sources, uses, and molecular mechanisms for thermostability, *Microbiol. Mol. Biol. Rev. 65*, 1−43.
26. Copley, R. R., and Burton, G. J. (1994) A structural analysis of phosphate and sulphate binding sites in proteins. Estimation of propensities for binding and conservation of phosphate binding sites, *J. Mol. Biol. 242*, 321−329.
27. Martin, D. D., Ciulla, R. A., and Roberts, M. F. (1999) Osmoadaptation in archaea, *Appl. Environ. Microbiol. 65*, 1815−1825.
28. Haney, P., Konisky, J., Koretke, K. K., Luthey-Schulten, Z., and Wolynes, P. G. (1997) Structural basis for thermostability and identification of potential active site residues for adenylate kinases from the archaeal genus *Methanococcus*, *Proteins: Struct., Funct., Genet. 28*, 117−130.
29. Thompson, M. J., and Eisenberg, D. (1999) Transproteomic evidence of a loop-deletion mechanism for enhancing protein thermostability, *J. Mol. Biol. 290*, 595−604.
30. Garcia-Viloca, M., Gao, J., Karplus, M., and Truhlar, D. G. (2004) How enzymes work: Analysis by modern rate theory and computer simulations, *Science 303*, 186−195.

BI048267O